

# Enabling the high capacity of lithium-rich anti-fluorite lithium iron oxide by simultaneous anionic and cationic redox

Chun Zhan<sup>1</sup>, Zhenpeng Yao<sup>2</sup>, Jun Lu<sup>1\*</sup>, Lu Ma<sup>3</sup>, Victor A. Maroni<sup>1</sup>, Liang Li<sup>4</sup>, Eungje Lee<sup>1</sup>, Esen E. Alp<sup>3</sup>, Tianpin Wu<sup>3</sup>, Jianguo Wen<sup>4</sup>, Yang Ren<sup>3</sup>, Christopher Johnson<sup>1</sup>, Michael M. Thackeray<sup>1</sup>, Maria K. Y. Chan<sup>4</sup>, Chris Wolverton<sup>2\*</sup> and Khalil Amine<sup>1\*</sup>

**Anionic redox reactions in cathodes of lithium-ion batteries are allowing opportunities to double or even triple the energy density. However, it is still challenging to develop a cathode, especially with Earth-abundant elements, that enables anionic redox activity for real-world applications, primarily due to limited strategies to intercept the oxygenates from further irreversible oxidation to O<sub>2</sub> gas. Here we report simultaneous iron and oxygen redox activity in a Li-rich anti-fluorite Li<sub>5</sub>FeO<sub>4</sub> electrode. During the removal of the first two Li ions, the oxidation potential of O<sup>2-</sup> is lowered to approximately 3.5 V versus Li<sup>+</sup>/Li<sup>0</sup>, at which potential the cationic oxidation occurs concurrently. These anionic and cationic redox reactions show high reversibility without any obvious O<sub>2</sub> gas release. Moreover, this study provides an insightful guide to designing high-capacity cathodes with reversible oxygen redox activity by simply introducing oxygen ions that are exclusively coordinated by Li<sup>+</sup>.**

Conventional cathode materials employed in lithium-ion batteries are generally lithiated transition metal (TM) oxide compounds. These materials store and release electrical energy when Li ions are extracted and inserted with charge compensated by redox reactions of the TM cations, respectively<sup>1</sup>. The specific capacity (mAh g<sup>-1</sup>) of these cathodes, therefore, is limited by the number of electrons per TM cation that can participate in the redox reactions and the relatively high atomic weight of the TM oxide host. Recently, the exclusive dependence on TM cations as the redox centre in the cathode has been challenged by the discovery of oxygen redox reactivity in Li-excess layered oxides<sup>2–8</sup>. The opportunity has thus arisen to boost the capacity and energy density of lithium-ion batteries if the anionic and cationic redox activity can be enabled at the same potential<sup>9,10</sup>. However, it is challenging to develop anionic-redox-based cathodes with acceptable cycle performance. The key issue is the irreversible O<sub>2</sub> gas release due to the instability of oxygenates (that is, O<sup>-</sup> or O<sub>n</sub><sup>2-</sup>) generated in the solid state. Several studies have demonstrated stabilized oxygenate species in cathode materials using expensive 4d or 5d TM ions such as Ir and Ru<sup>2,3,8,10</sup>. Nevertheless, low-cost 3d TM oxides are desirable to achieve highly reversible oxygen redox in practical applications, which requires an understanding of the mechanisms underpinning the anionic redox chemistry in this category of materials.

In principle, Li<sub>2</sub>O with the anti-fluorite structure maximally exploits the anionic redox, as it uses only oxygen ions to provide the charge-compensating electrons in the lithiation/delithiation reaction: Li<sub>2</sub>O ↔ 0.5Li<sub>2</sub>O<sub>2</sub> + Li<sup>+</sup> + e<sup>-</sup> (ref. 11). The direct Li<sub>2</sub>O/Li<sub>2</sub>O<sub>2</sub> conversion requires a catalyst to promote the electrochemical reaction because of the low electrochemical activity and poor electronic conductivity of lithium oxides. The release of O<sub>2</sub> is often associated with this reaction due to the metastability of the delithiated Li<sub>2</sub>O (ref. 12).

Prior studies show that the potential of the oxygen redox reaction of Li<sub>2</sub>O/Li<sub>2</sub>O<sub>2</sub>/LiO<sub>2</sub> is as low as ~3.0 V versus Li<sup>+</sup>/Li (refs 11–14). This value is comparable to the potential of several 3d TM redox reactions, offering the possibility of simultaneous cationic and anionic redox in TM-substituted anti-fluorite compounds. Indeed, it has been shown that the ionic and electronic conductivity, and electrochemical activity, are enhanced on substituting some of the Li ions with TM in Li-rich, defect anti-fluorite compounds such as Li<sub>5</sub>FeO<sub>4</sub>, Li<sub>6</sub>CoO<sub>4</sub> and Li<sub>6</sub>MnO<sub>4</sub> (refs 15–19). The anti-fluorite structure offers high potential capacity due to the rich Li ion content (over 5 per transition metal ion). For instance, Li<sub>5</sub>FeO<sub>4</sub> (LFO) delivers a theoretical capacity over 700 mAh g<sup>-1</sup> when charging to 4.7 V versus Li<sup>+</sup>/Li, amounting to an electrochemical extraction of about 4 Li<sup>+</sup> ions per Fe<sup>3+</sup> ion<sup>14,18–21</sup>. As it is unrealistic to expect that four electrons can be removed from a single Fe<sup>3+</sup> ion, anionic (O<sup>2-</sup>) oxidation has been suggested but without quantitative analysis or clear confirmation<sup>20–22</sup>. Despite previous studies of the electrochemical properties of LFO, little is known about the nature of the oxygen redox including the electrochemical potential, the reversibility, and the interplay of Fe and O redox.

Herein, we report the realization of simultaneous anionic and cationic redox in anti-fluorite structures, exemplified by Li<sub>5</sub>FeO<sub>4</sub>, at the same potential. Highly reversible anionic redox reactivity with no obvious oxygen release was enabled in this Earth-abundant iron-based oxide under a controlled voltage range. We also present a clear and quantitative picture of the structural and composition evolution of the LFO by ex situ and in situ X-ray diffraction (XRD), Raman, pressure measurement, differential electrochemical mass spectrometry (DEMS), X-ray absorption near-edge spectra (XANES), and first-principles calculations. Simultaneous oxidation of Fe<sup>3+</sup> to Fe<sup>4+</sup> and O<sup>2-</sup> to O<sup>-</sup> was observed at approximately 3.5 V versus Li<sup>+</sup>/Li during the extraction of the first two Li ions

<sup>1</sup>Chemical Sciences and Engineering Division, Argonne National Laboratory, Argonne, IL, USA. <sup>2</sup>Material Science and Engineering Department, Northwestern University, Evanston, IL, USA. <sup>3</sup>X-ray Science Division, Argonne National Laboratory, Argonne, IL, USA. <sup>4</sup>Centre for Nanoscale Materials, Argonne National Laboratory, Argonne, IL, USA. Chun Zhan and Zhenpeng Yao contributed equally to this work. \*e-mail: [junlu@anl.gov](mailto:junlu@anl.gov); [c-wolverton@northwestern.edu](mailto:c-wolverton@northwestern.edu); [amine@anl.gov](mailto:amine@anl.gov)

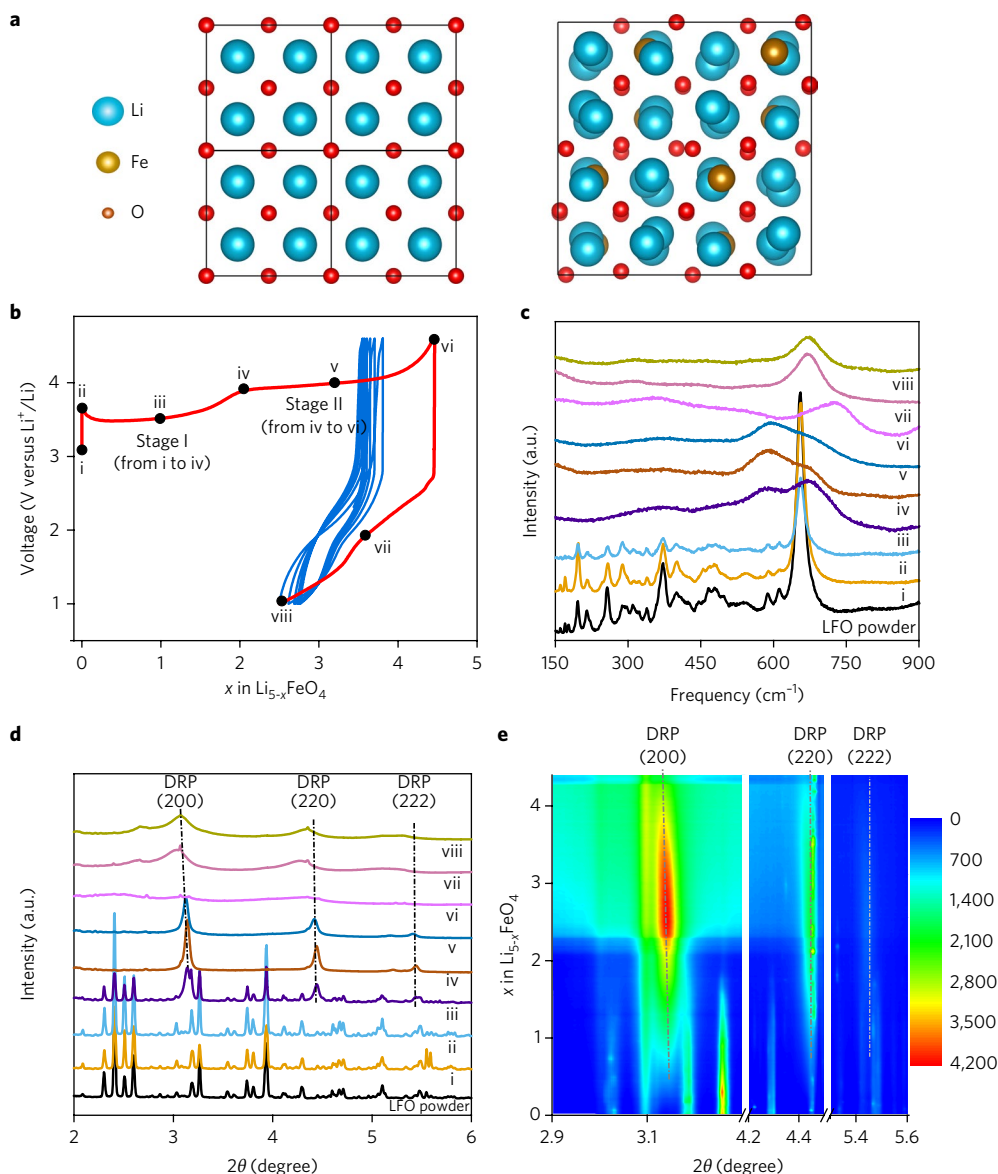


**Fig. 1 | Phase conversion of LFO during electrochemical cycling.** **a**, Structure of a  $2 \times 2 \times 2$   $\text{Li}_2\text{O}$  supercell and a  $\text{Li}_5\text{FeO}_4$  unit cell both in the [100] view. **b**, The charge–discharge behaviour of LFO in the first six cycles between 4.7 V and 1 V (first cycle as a red line and the following five cycles in blue). **c, d**, The ex situ Raman spectra obtained with a 633 nm laser (**c**) and ex situ high-energy XRD patterns (**d**) collected at different states of charge and discharge corresponding to the points in **a** (labelled as points i–viii). The pristine LFO powder and the cathode collected at points i and ii show typical features of the anti-fluorite  $\text{Li}_5\text{FeO}_4$ , with the prominent band at about  $660 \text{ cm}^{-1}$  and multiple bands at lower frequency according to ref. <sup>25</sup>. The fitting of Raman spectra at point iii and refinement of XRD patterns are given in Supplementary Fig. 1. **e**, 2D contour of in situ XRD patterns collected in the first charge, illustrating the continuous evolution of XRD patterns from i to viii in **d**. The vertical dashed lines in **d** and **e** label the diffraction peaks indexed to the (200), (220) and (222) planes of the disordered rocksalt phase (DRP).

from LFO. After the initial extraction of two Li ions, the iron and oxygen redox couples are highly reversible within the solid state in subsequent cycles between 1.0 and 3.8 V versus  $\text{Li}^+/\text{Li}$ . A Li-excess  $\text{Li}_6\text{O}$  configuration, identified by density functional theory (DFT) calculations, plays a key role in enabling the reversible  $\text{O}^-/\text{O}^{2-}$  redox behaviour. Our findings further the understanding of the oxygen redox mechanism and help in the design of low-cost 3d TM oxide-based high-energy-density cathode materials.

### Phase conversion of LFO during electrochemical cycling

The crystal structure of  $\text{Li}_5\text{FeO}_4$  can be viewed as substituting 24  $\text{Li}^+$  ions with 8  $\text{Fe}^{3+}$  ions and 16 cation vacancies in a  $2 \times 2 \times 2$   $\text{Li}_2\text{O}$  supercell (Fig. 1a). The charge–discharge behaviour of LFO

between 4.7 and 1.0 V is plotted in Fig. 1b. The initial charging curve exhibits two plateaux at about 3.5 V and 4.0 V, denoted stage I and stage II, respectively. This charging curve is consistent with previous literature<sup>16,20,23,24</sup>, but the subsequent discharging and cycling curves have rarely been discussed before. In the first discharge to a potential as low as 1.0 V, two tilted plateaux at about 2.2 V and 1.5 V can be observed corresponding to the ‘insertion’ of 1 Li ion at each plateau. The first charge to 4.7 V is electrochemically irreversible under the operating conditions employed here. In the following cycles, neither of the plateaux at 3.5 V and 4.0 V is recovered; instead, the charging and discharging curves show a plateau at about 2.5 V, and the capacity fades rapidly in the first five cycles.

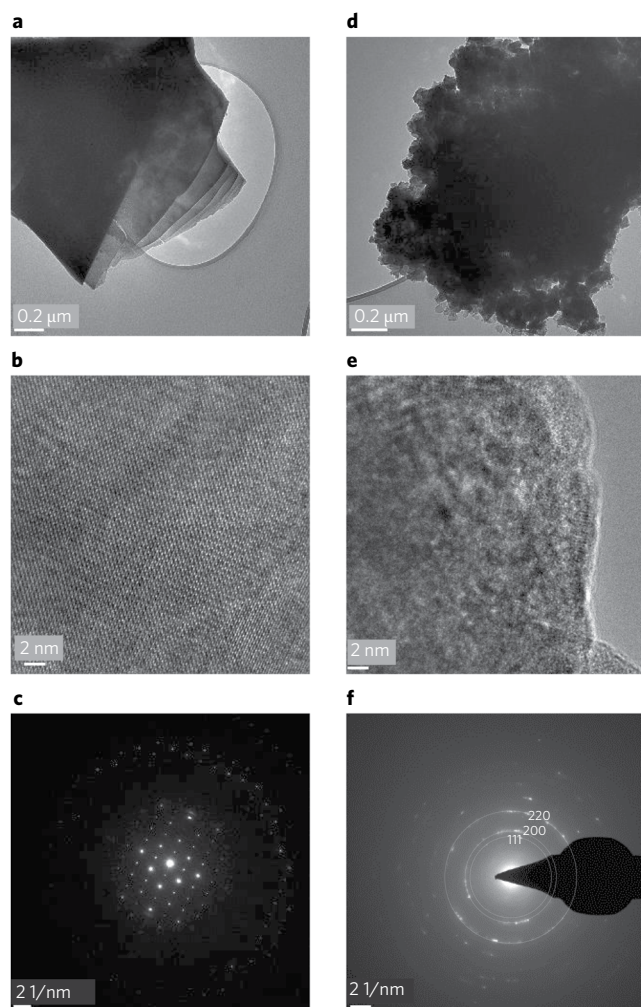


**Fig. 2 | Morphology and structure change of  $\text{Li}_5\text{FeO}_4$  during the first charge.** **a–f**, Low-resolution TEM image (**a,d**), high-resolution TEM image (**b,e**) and SAED pattern (**c,f**) of pristine  $\text{Li}_5\text{FeO}_4$  (**a–c**) and the sample charged to 3.8 V after the removal of two Li ions (**d–f**). It can be observed clearly that the micrometer-size LFO particles break into nanoparticles due to the delithiation. The SAED pattern of the delithiated LFO is indexed by the typical cubic phase structure, with diffuse rings generated by the nanoparticles.

LFO electrodes at different states of charge in the first cycle (labelled i to viii in Fig. 1b) were harvested for ex situ Raman and XRD analyses to determine the crystal phase conversion correlated with the plateaux, as shown in Fig. 1c,d, respectively. The fitting of the Raman spectrum at point iii and the refinement of the XRD patterns at points i, iv and v are shown in Supplementary Fig. 1 and Supplementary Table 1. Both the ex situ Raman and XRD profiles show that the initial LFO with an orthorhombic structure (space group of  $Pbca$ ) converted completely to a disordered rocksalt phase (DRP) at the 3.5 V plateau with the removal of two Li ions (from point i to iv in Fig. 1b)<sup>25</sup>. The two-phase coexistence can be observed in the middle of the plateau (point iii in Fig. 1b) as shown by the XRD pattern (Fig. 1d). Continuous phase conversion in the first charge is demonstrated in the two-dimensional (2D) contour of the in situ XRD patterns (Fig. 1e). Gradual fading of the original anti-fluorite phase and growth of the DRP can be observed when  $0 < x < 2$ .

Charging of LFO beyond two Li ions on the 4.0 V plateau has been reported previously<sup>20</sup>, but the mechanistic details of the reaction

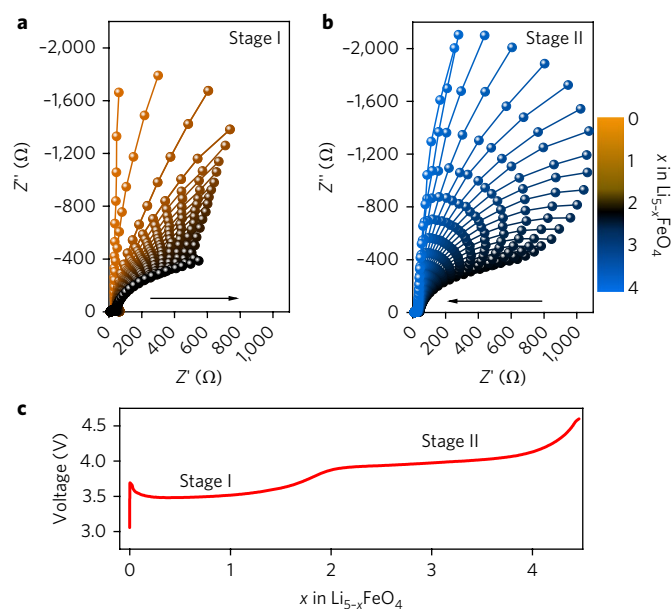


**Fig. 3 | In situ electrochemical impedance spectra of  $\text{Li}_{5-x}\text{FeO}_4$  during the first charge.** **a–c**, The EIS plots collected during charging stage I (**a**) and stage II (**b**) as denoted in the voltage profile of the first charge of LFO to 4.7 V (**c**). The colour of the lines and spheres represents the number of Li ions removed from the cathode, as demonstrated by the colour scale bar on the right. The arrows in **a** and **b** show that the impedance of LFO decreases at the 3.5 V plateau but increases at the 4.0 V plateau. The EIS measurements were performed using a three-electrode cell with LFO as the working electrode, a Li wire as the reference electrode and a Li metal foil as the counter electrode. In this way, the impedance contribution of the Li metal anode can be eliminated.

were not elucidated. Here, both the ex situ and in situ XRD patterns show that the DRP remains as the dominant phase on the 4.0 V plateau. The peaks of the DRP grow stronger at the beginning of the 4.0 V plateau ( $2 < x < 2.5$ ), then start to get broader and weaker when  $x > 2.5$ , and eventually become flattened at the end of charging. The XRD patterns of the DRP appear again in the first discharge, but the anti-fluorite phase cannot be recovered, confirming that deep delithiation of LFO is irreversible.

High-resolution images from transmission electron microscopy (TEM) helped explain the evolution of the XRD patterns, as shown in Fig. 2. The pristine LFO consists of well-crystallized particles of about 1  $\mu\text{m}$  in size, with the selected-area electron diffraction (SAED) pattern showing a typical single-crystal character (Fig. 2a–c). In contrast, after the removal of two Li ions, the single crystal of LFO breaks into nanoparticles of about 10 nm in size with the overall shape maintained (Fig. 2d,e). The SAED pattern indicates a polycrystalline character of the particle, and the diffraction rings are well correlated with the peaks in the XRD pattern at point iv.

The fracture of the active particles greatly increases the interface area between the cathode and electrolyte, which should lead to the impedance decrease of the LFO cathode in the first plateau. This trend is observed in the in situ electrochemical impedance spectra in Fig. 3. Other possible reasons for this impedance decrease include the enhanced charge conductivity due to the initial delithiation and the electronic structure change of iron and oxygen ions. The impedance of the cathode reaches the lowest level at the end of the first plateau and then increases gradually with further delithiation at the second plateau. A deeper exploration into the electrochemistry in the delithiation process is required to understand this

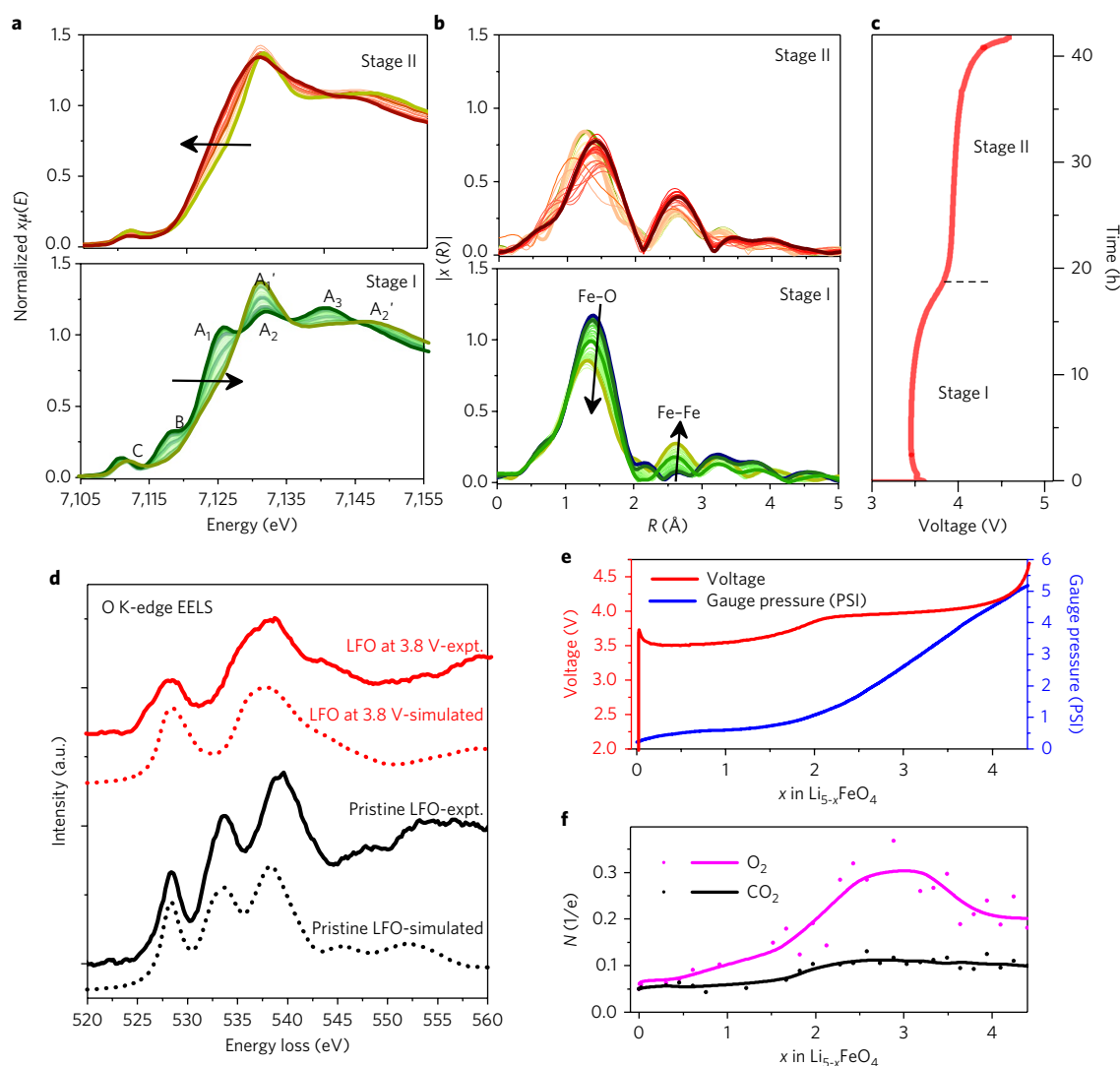


**Fig. 4 | Evolution of iron and oxygen in the first charge.** **a–c**, In situ Fe K-edge XANES (**a**) and EXAFS (**b**) of LFO during the first charge to 4.7 V, corresponding to the stages denoted on the charging curve (**c**). The decrease of the shoulder peak B and the pre-edge peak C, as well as the gradual change of the three main peaks ( $A_1$ ,  $A_2$  and  $A_3$  to  $A_1'$  and  $A_2'$ ), originated from the conversion of the  $\text{FeO}_4$  tetrahedron in the pristine LFO to the  $\text{FeO}_6$  octahedron in the DRP. The arrows in **a** show the shift of the main edge in the two stages, while the arrows in **b** show the decrease of the Fe–O peak and the increase of the Fe–Fe peak during charging stage I. **d**, Experimentally collected and simulated ex situ O K-edge EELS of  $\text{Li}_{5-x}\text{FeO}_4$  when  $x=0$  and 2 in the first charge. The simulations were performed using the crystal structure obtained from the experimental results, and thus the calculated shifting and shape variation of the peaks involve both the structural evolution and O redox. **e**, In situ pressure measurement showing the gauge pressure value inside the cell (blue line) corresponding to the charging voltage profile (red line) in the first cycle. **f**, Quantitative DEMS data for  $\text{O}_2$  and  $\text{CO}_2$  released in the LFO/Li cell in the first charge to 4.7 V.  $N$  (per electron) denotes the number of gas molecules generated by each electron. The lines show the smoothed curves using a fast Fourier transform filter.

V-shape evolution of impedance, which will be discussed in detail in the ‘Simultaneous cationic and anionic redox’ section.

### Cationic and anionic oxidation during the first charge

Figure 4a shows the in situ Fe K-edge XANES of LFO during the first charge to 4.7 V, and the quantitative analysis of the oxidation state of Fe by linear combination fitting is presented in Supplementary Fig. 2a. In stage I (charge to 3.5 V), the edge position of the main peak  $A_1$ , which is related to the oxidation state of Fe, shifted to higher energy ( $A_1'$ ) due to the oxidation of  $\text{Fe}^{3+}$  to  $\text{Fe}^{(3+\delta)+}$  ( $\delta \approx 0.5$ ) with extraction of the first two  $\text{Li}^+$  ions. This is an indirect indication that some other type of redox reaction is active, as  $\delta$  should be 2 if the Li removal is fully charge-compensated by the Fe ion. The shoulder peak B and the strong pre-edge peak C are signatures of  $\text{FeO}_4$  tetrahedral coordination<sup>20,24</sup>. The pre-edge

is partly caused by a quadrupole-allowed Fe 1s to 3d transition, which is also evident in the octahedral coordination, just not as strongly as in the tetrahedral coordination. The decrease in the intensity of peaks B and C, as well as the gradual change of the three main peaks ( $A_1$ ,  $A_2$  and  $A_3$  to  $A_1'$  and  $A_2'$ ), originated from the conversion of the  $\text{FeO}_4$  tetrahedron in the pristine LFO to the  $\text{FeO}_6$  octahedron in the DRP<sup>24</sup>. The disappearance of the  $\text{FeO}_4$  tetrahedron is also evident in the Raman spectra (Fig. 1c). In contrast, during stage II, the edge position of peak A shifted to lower energy, indicating that Fe was reduced during further removal of  $\text{Li}^+$  without coordination change. Again, the reduction of Fe during charge indicates that some other species is being oxidized (that is, O ions). This result is consistent with the ex situ Fe Mössbauer spectra shown in Supplementary Fig. 2b and Supplementary Table 2.

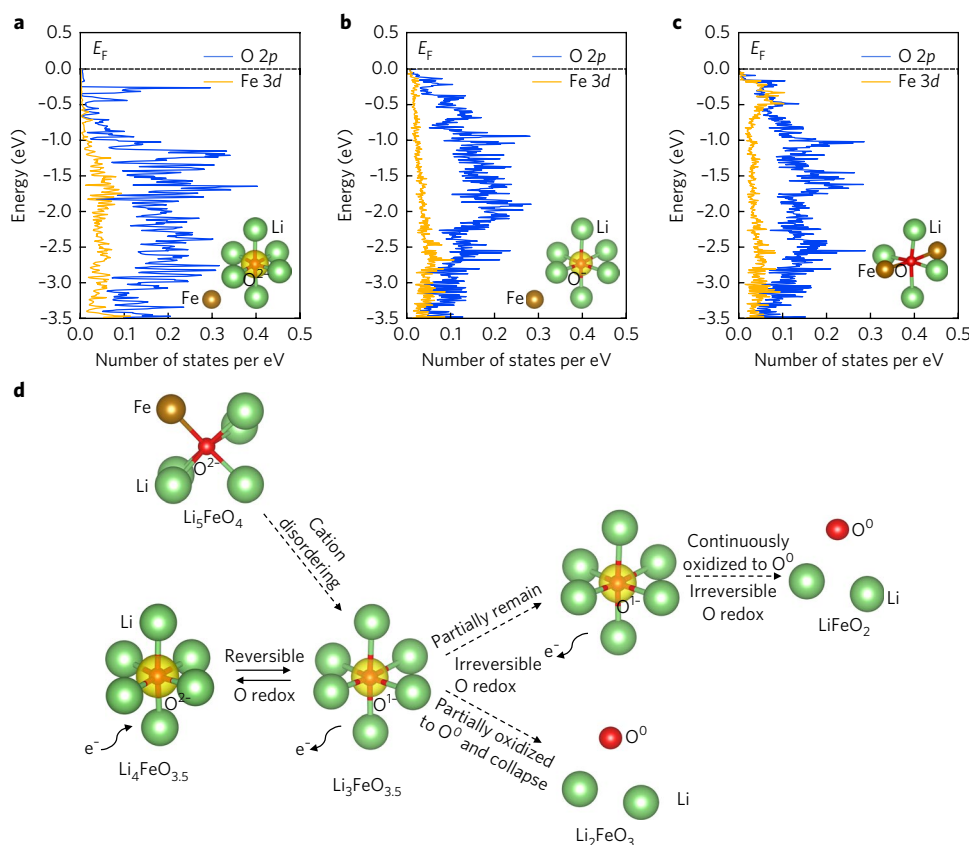


**Fig. 5 | Effect of  $Li_6-O$  configurations on the electronic states of O ions in cation DRPs.** The  $Li_6-O$  configurations lead to labile oxygen states.

**a–c**, pDOS of the O 2p orbitals and Fe 3d orbitals of  $O^{2-}$  ions in the  $Li_6-O$  configurations and nearest Fe ions in cation-disordered  $Li_4FeO_{3.5}$  (**a**),  $O^{1-}$  ions in the  $Li_6-O$  configuration and nearest Fe ions in cation-disordered  $Li_3FeO_{3.5}$  (**b**) and  $O^{2-}$  ions in Li/Fe-coordinated O configurations and nearest Fe ions in cation-disordered  $Li_3FeO_{3.5}$  (**c**). Insets: isosurfaces of the charge density (yellow) around the oxygen ions in the energy range of 0 to  $-1.0$  eV. All energies are expressed relative to Fermi energy (dashed black lines). Increased pDOS can be found near the Fermi level for the O ions coordinated by six Li, which originates from the particular  $Li_6-O$  configuration. **d**, Schematic of the role played by the  $Li_6-O$  configurations during the (de)lithiation of LFO. The irreversible delithiation from  $Li_3FeO_{3.5}$  to  $Li_2FeO_3$  and  $LiFeO_2$  is accompanied by the oxidation of  $O^{1-}$  to  $O^0$  and subsequent elimination of the  $Li_6-O$  configurations. Meanwhile, the  $O^{1-}$  ions in these  $Li_6-O$  configurations can be reversibly reduced to  $O^{2-}$  on further lithiation instead of delithiation. Thus, the  $O^-/O^{2-}$  redox can be reversible when the delithiation does not proceed beyond the point where  $Li_6-O$  configurations are eliminated.

The Fe K-edge extended X-ray absorption fine structure (EXAFS) was measured to investigate bond distances and the local structure surrounding the Fe atoms. Figure 4b shows the Fourier transform of the  $k^2$ -weighted EXAFS. The peak at  $\sim 1.5$  Å corresponds to the Fe–O bond. The Fe–O bond in pristine LFO is longer than that in the  $FeO_6$  unit, which demonstrates tetrahedral coordination of Fe in LFO<sup>24</sup>. The Fe–O bond is gradually shortened at the end of stage I, that is, approaching the Fe–O bond length of the  $FeO_6$ . The Fe–O bond distance did not change in an obvious manner during stage II.

When comparing the number of Li ions extracted versus the valence change of Fe during the two plateaux, we inferred that about  $(2-\delta)$  electrons per formula unit (or per Fe) are required from O atoms in the 3.5 V plateau, and another  $(2+\delta)$  electrons are required in the 4.0 V plateau. Therefore, the average valences of the four oxygen ions are expected to change from  $-2$  to  $-(1.5+0.25\delta)$  and then to  $-1$ . The evolution of oxygen valence in the solid cathode was traced by ex situ O K-edge electron energy-loss spectroscopy (EELS) of pristine LFO and LFO charged to 3.8 V (Fig. 4d). Three peaks near 528.4 eV, 533.6 eV and 539.4 eV are observed in the O K-edge spectrum of pristine LFO, whereas the spectrum for LFO after charging across the 3.5 V plateau exhibits only two board peaks at 528.4 eV and 538.2 eV. The drastic change in the EELS spectra shows the response of oxygen electronic structure to Li

electrochemical extraction, which may possibly be linked to a change in the oxygen bonding environment or oxygen redox. The experimentally observed O K-edge EELS spectra of pristine and delithiated LFO were confirmed by O core-level spectrum simulation.

Figure 4e,f shows the in situ pressure measurement and quantitative DEMS data of the LFO/Li cell in the first charge to 4.7 V. The pressure increase shows that minor gas release is observed during the charge plateau at 3.5 V. Subsequently, a large amount of gas is released during the 4.0 V plateau. The calculation from DEMS data shows that about 0.1  $O_2$  gas molecules are released per electron on the first plateau. This number increases rapidly to about 0.3  $O_2$  per electron when the potential rises to 4.0 V.

### Simultaneous cationic and anionic redox

The composition of the product generated at the 3.5 V plateau was assumed to be  $Li_xFe^{(4-\alpha)+}O_2$  by the authors of ref. <sup>24</sup>, but the (111)/(200) peak intensity ratio for this composition should be much higher than that in their observed XRD profiles. They attributed the ‘mismatch’ of  $I(111)$  to lattice distortion. This ‘mismatch’ is also observed here and, indeed, can be eliminated by reducing the Fe/O ratio in the DRP in the XRD Rietveld refinements (Supplementary Fig. 1). The refined occupancies of the atoms yield a stoichiometry of  $Li_3FeO_{3.5}$  for the DRP after the removal of two Li ions

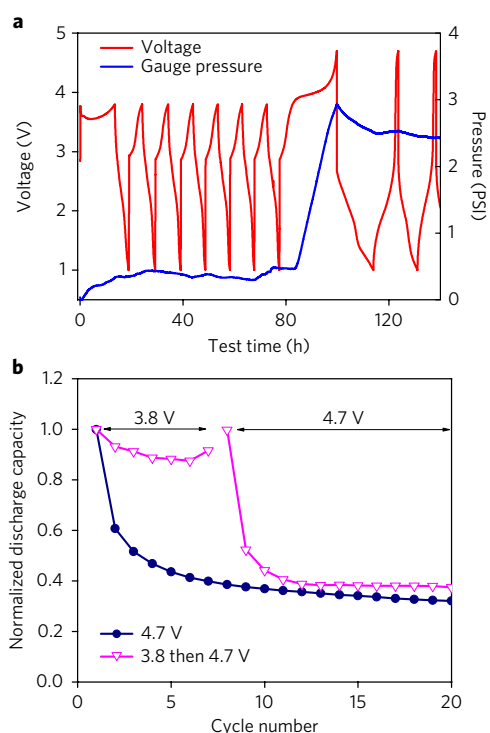
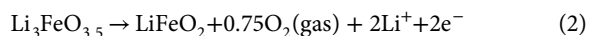
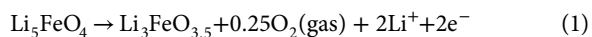


**Fig. 6 | Onset voltage for O<sub>2</sub> gas release from Li<sub>5</sub>FeO<sub>4</sub>** **a**, The voltage profile (red line) and the in situ pressure (blue line) of the Li<sub>5</sub>FeO<sub>4</sub>/Li cells during cycles with an upper cutoff voltage of 3.8 V. **b**, Performance of Li<sub>5</sub>FeO<sub>4</sub> when cycled with a cutoff voltage of 3.8 V and then 4.7 V (magenta line, corresponding to cell in **a** versus at 4.7 V from the beginning (navy line)).

(Supplementary Table 1), which is consistent with the DFT simulations (Supplementary Notes).

The O K-edge spectra for both Li<sub>5</sub>FeO<sub>4</sub> and Li<sub>3</sub>FeO<sub>3.5</sub> are simulated on the basis of the DFT-predicted structures (Supplementary Figs. 3 and 4), using the OCEAN code implementing the Bethe–Salpeter equation approach<sup>26,27</sup> (details in Supplementary Notes). The simulated spectra are in excellent agreement with the EELS spectra (Fig. 4d). To determine the electronic origin of each peak, we also compared the simulated spectra with the projected ground-state density of states (DOS) of Li<sub>5</sub>FeO<sub>4</sub> and Li<sub>3</sub>FeO<sub>3.5</sub>, as shown in Supplementary Fig. 5. The three peaks in the Li<sub>5</sub>FeO<sub>4</sub> spectrum are attributed to electronic transitions from the O 1s core level to the unoccupied Fe 3d states (of Fe<sup>3+</sup> in tetrahedral sites) mixed with O 2p, and to delocalized O p states that are mixed with Fe states at higher energies<sup>28</sup>. Similarly, the two peaks in the Li<sub>3</sub>FeO<sub>3.5</sub> spectrum can tentatively be assigned to the empty 3d states of Fe<sup>3+</sup> and Fe<sup>4+</sup> that hybridize with O 2p state, and also to O p states mixed with Fe states in the extended region. The fidelity of the Li<sub>3</sub>FeO<sub>3.5</sub> structural model obtained from DFT calculation is thus corroborated by the close resemblance between the experimental and simulated O core-level spectra.

Therefore, the removal of the four Li ions can be expressed as follows:



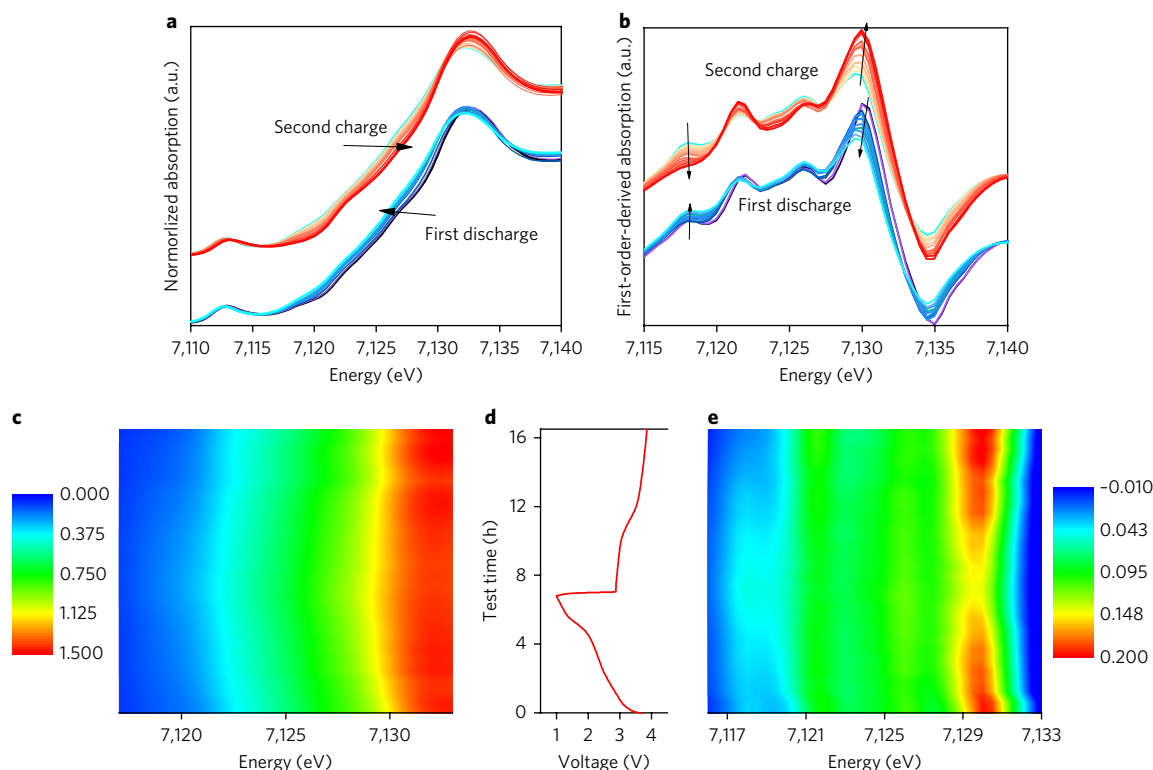
The number of O<sub>2</sub> molecules released per electron is 0.125 at 3.5 V (equation (1)) and 0.375 at 4 V (equation (2)), which is close

to the DEMS results. On the basis of the EELS and XANES results mentioned above, Li<sub>3</sub>FeO<sub>3.5</sub> can be expressed as Li<sub>3</sub>(Fe<sup>3+</sup><sub>0.5</sub>Fe<sup>4+</sup><sub>0.5</sub>) (O<sup>2-</sup><sub>3</sub>O<sup>-</sup><sub>0.5</sub>), which is also consistent with charge states deduced from DFT (see below and Supplementary Fig. 6). According to this electrochemistry, the lowest impedance of the cathode at around  $x=2$  (Fig. 3) could originate from the high electrochemical activity of the Fe<sup>4+</sup> and O<sup>-</sup> in the Li<sub>3</sub>FeO<sub>3.5</sub>. In total, the removal of the first two Li<sup>+</sup> ions is charge-compensated by one electron from the formation of oxygen vacancies (0.5 O<sup>2-</sup> to 0.25 O<sub>2</sub>), 0.5 electrons from oxygen redox in the solid state (0.5 O<sup>2-</sup> to 0.5 O<sup>-</sup>) and 0.5 electrons from Fe redox (0.5 Fe<sup>3+</sup> to 0.5 Fe<sup>4+</sup>). Subsequently, 0.75 O<sub>2</sub> gas per formula unit is released from 0.5 O<sup>-</sup> plus one O<sup>2-</sup>, providing two electrons for the removal of another two Li ions and 0.5 electrons for the reduction of 0.5 Fe<sup>4+</sup> back to 0.5 Fe<sup>3+</sup>.

When comparing our results for LFO with those of layered oxides reported previously, we find that the potential for oxygen redox (~3.5 V versus Li<sup>+/</sup>Li) and O<sub>2</sub> release (4.0 V versus Li<sup>+/</sup>Li) in the LFO cathode is lower than that in the layered oxides (4.2 V and 5 V versus Li<sup>+/</sup>Li, respectively, for Li<sub>4</sub>FeSbO<sub>6</sub>)<sup>4</sup>. One possible reason for the more facile oxygen redox is the difference in the bonding or coordination environment of the oxygen ions relative to the cation (Li/Fe)-disordered sub-lattice in the DRP. Unlike conventional cubic cathode materials, which are well ordered and have only a single local environment for oxygen ions, a variety of local oxygen environments exist in cation DRPs. Through systematically calculating and examining the DOS and charge/spin density around oxygen ions in various local environments using DFT, we demonstrate that the local configuration sensitively affects oxygen redox activity in LFO (Fig. 5). To determine the oxidation states of oxygen ions, we compared calculated magnetizations of oxygen ions with the number of unpaired electrons of the corresponding ions at each oxidation state (Supplementary Fig. 6). In the resulting Li<sub>3</sub>FeO<sub>3.5</sub> phase, DFT calculations show that all of the O<sup>-</sup> ions share a common ‘Li<sub>6</sub>-O’ configuration (Fig. 5d) with only Li ion coordination (first nearest neighbours) while the remaining oxygen ions stay as O<sup>2-</sup> with at least one Fe first nearest neighbour (Supplementary Fig. 7). The projected DOS (pDOS) of the oxygen 2p states and 3d states of the nearest iron ion for Li<sub>6</sub>-O- and Fe-coordinated configurations were examined and are shown in Fig. 5b,c. A much greater pDOS from the oxygen states than from the iron states immediately below the Fermi level is found for the O<sup>-</sup> ion coordinated with six Li ions (Fig. 5b). The origin of this increased DOS can be identified by visualizing the charge density around the oxygen ion for the energy range corresponding to the extraction of one electron (inset of Fig. 5b). Distinct from the previously reported local Li-excess ‘Li-O-Li’ configuration<sup>6</sup>, here we find that the O<sup>-</sup> in the local Li-excess environment originating from this particular Li<sub>6</sub>-O configuration can emit one labile electron and become O<sup>0</sup> on further delithiation of Li<sub>3</sub>FeO<sub>3.5</sub>. Our calculations indicate that the local coordination is responsible for oxygen redox (O<sup>2-</sup> to O<sup>-</sup>). We find that the irreversible delithiation from Li<sub>3</sub>FeO<sub>3.5</sub> to Li<sub>2</sub>FeO<sub>3</sub> and LiFeO<sub>2</sub> is accompanied by gradual oxidation of O<sup>-</sup> to O<sup>0</sup> and subsequent elimination of the ‘oxygen redox’-specific Li<sub>6</sub>-O configurations (Fig. 5d). Nevertheless, the O<sup>-</sup> ions in these Li<sub>6</sub>-O configurations should be reversibly reduced to O<sup>2-</sup> on further lithiation instead of delithiation. Thus, the calculations suggest that the O<sup>-</sup>/O<sup>2-</sup> redox can be reversible when the cutoff voltage for charging is lowered such that delithiation does not proceed to the point where Li<sub>6</sub>-O configurations are eliminated (and O<sup>0</sup> is formed). We will discuss this hypothesis in the following section.

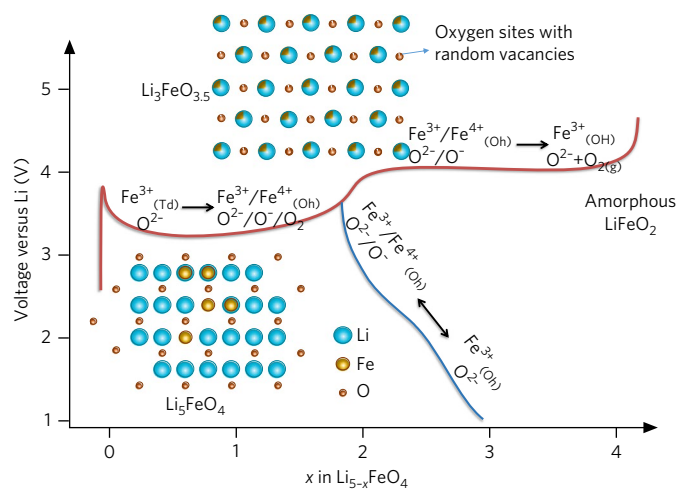
### Reversibility of the anionic and cationic redox

Figure 6 shows the cycle performance and the in situ gas release measurements for LFO during cycling between 1.0 and 3.8 V after the extraction of the first two Li ions in the first charge. As



**Fig. 7 | Reversibility of the  $\text{Fe}^{3+}/\text{Fe}^{4+}$  redox couple.** **a, b**, Normalized (**a**) and first-order-derived (**b**) in situ Fe K-edge XANES collected on the LFO cathode during the first discharge and the second charge after the initial charge to 3.8 V. **c–e**, 2D contour of **a** (**c**) and **b** (**e**), corresponding to the charge–discharge curve (**d**).

shown in Fig. 6a, no obvious gas release occurred when the cell was cycled with the upper voltage limited to 3.8 V. On the contrary, the gas pressure increased every time the cell was charged to 4.0 V (Supplementary Fig. 8a). In addition, the noticeable gas release at



**Fig. 8 | Schematic of the structural change and redox reactions in  $\text{Li}_5\text{FeO}_4$  during electrochemical cycling.** For clarity, the structure of pristine  $\text{Li}_5\text{FeO}_4$  is simplified as the standard anti-fluorite structure by ignoring the position offsets of the atoms. The first charging voltage profile is plotted in red. The structure of the cathode material after discharging of  $\text{Li}_3\text{FeO}_{3.5}$  (shown as the blue curve) is demonstrated in Supplementary Fig. 8d, resulting from the refinement of the ex situ XRD pattern. As the octahedral sites are fully occupied in  $\text{Li}_3\text{FeO}_{3.5}$ , the lithiation of  $\text{Li}_3\text{FeO}_{3.5}$  occurs with the insertion of Li ions into the tetrahedral sites.

the 4.0 V plateau is maintained after several cycles between 3.8 V and 1.0 V, confirming that the oxygen ion redox couple stays in the solid cathode when it is cycled below 3.8 V after the first two-Li extraction. The cathode showed stable capacity when cycled with the upper voltage limit at 3.8 V, but not 4.7 V (Fig. 6b and Supplementary Fig. 8b).

To study the reversibility of the  $\text{Fe}^{3+}/\text{Fe}^{4+}$  redox couple, in situ Fe K-edge XANES were collected for the LFO cathode during the cycles after the first charge to 3.8 V, as shown in Fig. 7. During the discharge from 3.8 V to 1.0 V, the main Fe K-edge shifted back to around 7,130 eV, confirming the reduction from  $\text{Fe}^{(3+\delta)+}$  to  $\text{Fe}^{3+}$ . However, the typical tetrahedral  $\text{Fe}^{3+}$  peaks and edges of the original LFO (shown in Fig. 7a) were not recovered. This finding indicates that the octahedral  $\text{Fe}^{(3+\delta)+}$  in the DRP does not move back to a tetrahedral site (in the original LFO phase) after being reduced to  $\text{Fe}^{3+}$ . The irreversibility of the Fe redox in the first charge and discharge is consistent with the asymmetric voltage–capacity profile in the first cycle. On the other hand, after the first charge to 3.8 V, the Fe K-edge XANES shows a nearly symmetric pattern between the first discharge and the second charge, as demonstrated in the 2D contour graphs (Fig. 7c,d), indicating that  $\text{Fe}^{(3+\delta)+}/\text{Fe}^{3+}$  at the octahedral site can be reduced and oxidized reversibly.

According to the DFT simulations of the lithiated phase ( $\text{Li}_4\text{FeO}_{3.5}$ ), the pDOS from the  $2p$  states of the oxygen ions in the centre of the  $\text{Li}_6\text{–O}$  configurations, which are inherited from  $\text{Li}_3\text{FeO}_{3.5}$ , is confirmed to be greater than the pDOS from the  $3d$  states of the nearest iron ions (Fig. 5a). Corresponding labile electron extraction/insertion from these  $\text{Li}_6\text{–O}$  configurations enables reversible  $\text{O}^{2-}/\text{O}^-$  redox. As about one Li ion (corresponding to a capacity around  $170 \text{ mAh g}^{-1}$ ) is involved in the first discharge and the following cycling between 1.0 and 3.8 V, about 0.5 electron is provided by cationic redox ( $0.5 \text{ Fe}^{4+} \leftrightarrow 0.5 \text{ Fe}^{3+}$ ) and 0.5 electron is then provided by anionic redox ( $0.5 \text{ O}^- \leftrightarrow 0.5 \text{ O}^{2-}$ ).

## Discussion

Figure 8 summarizes the structural changes and redox reactions involved in the electrochemical cycling of LFO. With the removal of two Li ions on the 3.5 V plateau, Fe and Li ions migrate from tetrahedral sites to octahedral sites with a conversion from the anti-fluorite phase to a DRP. At the same time, part of the  $\text{Fe}^{3+}$  and part of the  $\text{O}^{2-}$  are oxidized to  $\text{Fe}^{4+}$  and  $\text{O}^-$ , together with the formation of some oxygen vacancies. The  $\text{Fe}^{4+}/\text{Fe}^{3+}$  and  $\text{O}^-/\text{O}^{2-}$  redox couples in the lattices are reversible with substantial capacity retention in the subsequent cycles when the upper potential is limited to 3.8 V. Charging beyond two Li ions results in the reduction of  $\text{Fe}^{4+}$  to  $\text{Fe}^{3+}$ , as well as  $\text{O}_2$  gas release.

The pursuit of breaking the capacity limits has recently turned the research focus to the anionic redox. Fundamental research has been carried out on stabilizing oxygenate species by using 4d or 5d metal ions via, for example, high M–O covalence; however, we believe that 3d metal oxides with lower cost and weight could be more practical in terms of real applications. The combined experimental and computational studies in this work demonstrate how the coordination structure and bonding environment enable reversible oxygen redox in the 3d metal oxides. The  $\text{Li}_2\text{O}$ -like anti-fluorite structure facilitates oxygen redox potential lower than 3.8 V, while the fully cationic disordered rocksalt phase generated in the charging stabilizes the oxygenate species (that is,  $\text{O}^-$ ) via the  $\text{Li}_6\text{O}$  configuration. In fact, the  $\text{Li}_6\text{O}$  configuration can be tuned by controlling the Li/TM disordering in the oxides, which could be readily followed by further studies to realize improved capacities and stability in different electrodes. This extensive understanding of oxygen redox in different coordination environments could enable new pathways to next-generation, high-energy cathode materials based on simultaneous anionic and cationic redox chemistry.

## Methods

**Material preparation and electrochemical tests.** Li-rich anti-fluorite  $\text{Li}_5\text{FeO}_4$  (LFO) powders were synthesized by solid-state synthesis in an Ar-filled glovebox (details reported elsewhere<sup>29</sup>). Electrochemistry tests were performed with 2032 coin cells assembled with a cathode material of 80% LFO, 10% carbon black and 5% polyvinylidene difluoride binder. The GenII electrolyte was used: 1.2 M  $\text{LiPF}_6$  in ethylene carbonate/ethyl methyl carbonate at a 3:7 ratio by weight. Unless specified otherwise, the cells were cycled with a constant current density of  $19 \text{ mA g}^{-1}$  (about 1/40 C for the first charge).

The in situ electrode electrochemical impedance spectra were collected with Li metal wire as the reference electrode, Li metal as the counter electrode and the LFO as the cathode, using a Solartron Analytical 1400 System. The a.c. amplitude was set at  $\pm 5 \text{ mV}$ , and the applied frequency range was between 100 kHz and 0.05 Hz. In situ pressure measurements were carried out in a home-modified system by connecting a pressure transducer (Omega) to the open end of a Swagelok-type cell. DEMS measurements were performed following the method described in detail elsewhere<sup>30</sup>. The system was built based on a mass spectrometer (HPR-40, Hiden Analytical). The mass spectrometer was calibrated by standard mixture gas of  $\text{CO}_2$ ,  $\text{O}_2$ , and  $\text{H}_2$  (2%, 5%, and 10%) in Ar. Before the testing, ultrahigh purity Ar was purged through the whole system and then the cell was isolated for gas accumulation. During the cell testing, the gas generated in the cell was accumulated for every 60 min and then pushed to the sample cross space by pure Ar. Then, the gas was further injected to the mass spectrometer to measure the partial pressures of Ar,  $\text{O}_2$  and  $\text{CO}_2$ . The pressure of the sample cross space was recorded by a pressure transducer (PX419-USBH), and the volume of the sample cross space was calibrated by known volume tubings.

**Material characterization.** High-energy synchrotron XRD measurements were carried out at the 11-ID-C beamline of the Advanced Photon Source (APS), Argonne National Laboratory. The wavelength of the X-ray is 0.11165 nm. The XRD patterns were collected in the transmission mode using a Perkin Elmer large-area detector. The collected 2D patterns were then integrated into conventional 1D patterns (intensity versus  $2\theta$ ) for final data analysis using the Fit2d software. The XRD Rietveld refinement was carried out with the Fullprof Suite 2012. Raman spectra were obtained using a Renishaw inVia Raman Microprobe. The spectra were excited with 633 nm radiation. Other details of the sample handling, spectra measurement, and data processing procedures are as described in ref. 25.

TEM images and SAED patterns were taken by a field-emission transmission electron microscope (FEI Titan 80-300ST) with a spherical and chromatic aberration imaging corrector working at 80 kV. Spherical and chromatic aberration correction enables the microscope to attain resolution better than 0.1 nm (measured by Young's fringes) at 80 kV.

X-ray absorption spectroscopy (XAS) measurements at the Fe K-edge were completed at the APS on the bending-magnet beamline 9-BM-B with an electron energy of 7 GeV and an average current of 100 mA. The incident beam was monochromatized by a Si(111) double-crystal monochromator. Harmonic rejection was accomplished with a 25% detune. The monochromator energy was calibrated with a Fe foil by setting the first derivative maxima to 7,110.75 eV. In situ XAS experiments were performed on the coin cells with a window of 3-mm diameter sealed with 50- $\mu\text{m}$ -thick Kapton tape in transmission mode. The cells were cycled with a MACCOR cycler. Data reduction and analysis were performed by using the ATHENA software<sup>31</sup>.

Ex situ Mössbauer spectroscopy was conducted on cycled electrodes. Cathode laminates at selected states of charge were removed from the coin cells and covered with Kapton tape to reduce effects from the outside environment. The measurements were performed in transmission geometry with a 20 mCi  $^{57}\text{mCo}$  in Rh source and a Peltier-cooled silicon detector. The isomer shift (measured relative to an  $\alpha\text{-Fe}$  foil) and the quadrupole splitting values were obtained by a least-squares fitting of the data using Lorentzian functions.

**DFT calculations.** First-principles calculations were performed using the Vienna Ab-initio Simulation Package<sup>32–35</sup> and the projector augmented wave potentials<sup>36</sup>. The generalized gradient approximation of Perdew–Becke–Ernzerhof<sup>37</sup> was used for the exchange–correlation functional. A plane-wave basis set with a cutoff energy of 520 eV and  $\Gamma$ -centered  $k$ -meshes with an approximate density of 8,000  $k$ -points per reciprocal atom was used in all calculations. The DFT +  $U$  method was used to treat Fe 3d ( $U_{\text{Fe}} = 4.0 \text{ eV}$ ) states following previous work<sup>22,38–41</sup>.

**Data availability.** The data that support the plots within this paper and other findings of this study are available from the corresponding author upon reasonable request

Received: 16 May 2017; Accepted: 23 October 2017;

Published online: 8 December 2017

## References

- Whittingham, M. S. Lithium batteries and cathode materials. *Chem. Rev.* **104**, 4271–4301 (2004).
- Sathiyar, M. et al. Reversible anionic redox chemistry in high-capacity layered-oxide electrodes. *Nat. Mater.* **12**, 827–835 (2013).
- McCalla, E. et al. Visualization of O–O peroxo-like dimers in high-capacity layered oxides for Li-ion batteries. *Science* **350**, 1516–1521 (2015).
- McCalla, E. et al. Understanding the roles of anionic redox and oxygen release during electrochemical cycling of lithium-rich layered  $\text{Li}_4\text{FeSbO}_6$ . *J. Am. Chem. Soc.* **137**, 4804–4814 (2015).
- Luo, K. et al. Charge-compensation in 3d-transition-metal-oxide intercalation cathodes through the generation of localized electron holes on oxygen. *Nat. Chem.* **8**, 684–691 (2016).
- Seo, D.-H. et al. The structural and chemical origin of the oxygen redox activity in layered and cation-disordered Li-excess cathode materials. *Nat. Chem.* **8**, 692–697 (2016).
- Sathiyar, M. et al. Electron paramagnetic resonance imaging for real-time monitoring of Li-ion batteries. *Nat. Commun.* **6**, 6276 (2015).
- Grimaud, A., Hong, W., Shao-Horn, Y. & Tarascon, J.-M. Anionic redox processes for electrochemical devices. *Nat. Mater.* **15**, 121–126 (2016).
- Freire, M. et al. A new active Li–Mn–O compound for high energy density Li-ion batteries. *Nat. Mater.* **15**, 173–177 (2016).
- Pearce, P. E. et al. Evidence for anionic redox activity in a tridimensional-ordered Li-rich positive electrode  $\beta\text{-Li}_2\text{IrO}_3$ . *Nat. Mater.* **16**, 580–586 (2017).
- Zhu, Z. et al. Anion-redox nanolithia cathodes for Li-ion batteries. *Nat. Energy* **1**, 16111 (2016).
- Okuoka, S.-i et al. A new sealed lithium-peroxide battery with a Co-doped  $\text{Li}_2\text{O}$  cathode in a superconcentrated lithium bis(fluorosulfonyl)amide electrolyte. *Sci. Rep.* **4**, 5684 (2014).
- Ogasawara, Y. et al. Charge/discharge mechanism of a new Co-doped  $\text{Li}_2\text{O}$  cathode material for a rechargeable sealed lithium-peroxide battery analyzed by X-ray absorption spectroscopy. *J. Power Sources* **287**, 220–225 (2015).
- Harada, K. et al. Electrochemical reactions and cathode properties of Fe-doped  $\text{Li}_2\text{O}$  for the hermetically sealed lithium peroxide battery. *J. Power Sources* **322**, 49–56 (2016).
- Narukawa, S. et al. Anti-fluorite type  $\text{Li}_6\text{CoO}_4$ ,  $\text{Li}_5\text{FeO}_4$ , and  $\text{Li}_6\text{MnO}_4$  as the cathode for lithium secondary batteries. *Solid State Ionics* **122**, 59–64 (1999).
- Imanishi, N. et al. Antifluorite compounds,  $\text{Li}_{5+x}\text{Fe}_{1-x}\text{Co}_x\text{O}_4$ , as a lithium intercalation host. *J. Power Sources* **146**, 21–26 (2005).



17. Noh, M. & Cho, J. Role of  $\text{Li}_2\text{CoO}_4$  cathode additive in Li-ion cells containing low coulombic efficiency anode material. *J. Electrochem. Soc.* **159**, A1329–A1334 (2012).
18. Lim, Y.-G. et al. Anti-fluorite  $\text{Li}_6\text{CoO}_4$  as an alternative lithium source for lithium ion capacitors: an experimental and first principles study. *J. Mater. Chem. A* **3**, 12377–12385 (2015).
19. Kirklin, S., Chan, M. K. Y., Trahey, L., Thackeray, M. M. & Wolverton, C. High-throughput screening of high-capacity electrodes for hybrid Li-ion-Li- $\text{O}_2$  cells. *Phys. Chem. Chem. Phys.* **16**, 22073–22082 (2014).
20. Johnson, C. et al.  $\text{Li}_2\text{O}$  removal from  $\text{Li}_3\text{FeO}_4$ : A cathode precursor for lithium-ion batteries. *Chem. Mater.* **22**, 1263–1270 (2010).
21. Trahey, L. et al. Activated lithium-metal-oxides as catalytic electrodes for Li- $\text{O}_2$  cells. *Electrochem. Solid-State Lett.* **14**, A64–A66 (2011).
22. Thackeray, M. M., Chan, M. K. Y., Trahey, L., Kirklin, S. & Wolverton, C. Vision for designing high-energy, hybrid Li ion/Li- $\text{O}_2$  cells. *J. Phys. Chem. Lett.* **4**, 3607–3611 (2013).
23. Hirano, A. et al. Electrochemical properties and Mössbauer effect of anti-fluorite type compound,  $\text{Li}_3\text{FeO}_4$ . *Solid State Ionics* **176**, 2777–2782 (2005).
24. Okumura, T., Shikano, M. & Kobayashi, H. Effect of bulk and surface structural changes in  $\text{Li}_3\text{FeO}_4$  positive electrodes during first charging on subsequent lithium-ion battery performance. *J. Mater. Chem. A* **2**, 11847–11856 (2014).
25. Maroni, V. A., Johnson, C. S., Rood, S. C. M., Kropf, A. J. & Bass, D. A. Characterization of novel lithium battery cathode materials by spectroscopic methods: The  $\text{Li}_{5+x}\text{FeO}_4$  system. *Appl. Spectrosc.* **67**, 903–912 (2013).
26. Gilmore, K. et al. Efficient implementation of core-excitation Bethe–Salpeter equation calculations. *Comput. Phys. Commun.* **197**, 109–117 (2015).
27. Vinson, J., Rehr, J. J., Kas, J. J. & Shirley, E. L. Bethe–Salpeter equation calculations of core excitation spectra. *Phys. Rev. B* **83**, 115106 (2011).
28. Mizokawa, T. et al. Role of oxygen holes in  $\text{Li}_2\text{CoO}_2$  revealed by soft X-ray spectroscopy. *Phys. Rev. Lett.* **111**, 056404 (2013).
29. Su, X. et al. A new strategy to mitigate the initial capacity loss of lithium ion batteries. *J. Power Sources* **324**, 150–157 (2016).
30. McCloskey, B. D., Bethune, D., Shelby, R., Girishkumar, G. & Luntz, A. Solvents' critical role in nonaqueous lithium–oxygen battery electrochemistry. *J. Phys. Chem. Lett.* **2**, 1161–1166 (2011).
31. Ravel, B. & Newville, M. ATHENA, ARTEMIS, HEPHAESTUS: data analysis for X-ray absorption spectroscopy using IFEFFIT. *J. Synchrotron Rad.* **12**, 537–541 (2005).
32. Kresse, G. & Hafner, J. Ab initio molecular dynamics for liquid metals. *Phys. Rev. B* **47**, 558–561 (1993).
33. Kresse, G. & Hafner, J. Ab initio molecular-dynamics simulation of the liquid-metal–amorphous-semiconductor transition in germanium. *Phys. Rev. B* **49**, 14251–14269 (1994).
34. Kresse, G. & Furthmüller, J. Efficiency of ab-initio total energy calculations for metals and semiconductors using a plane-wave basis set. *Comput. Mater. Sci.* **6**, 15–50 (1996).
35. Kresse, G. & Furthmüller, J. Efficient iterative schemes for ab initio total-energy calculations using a plane-wave basis set. *Phys. Rev. B* **54**, 11169–11186 (1996).
36. Blöchl, P. E. Projector augmented-wave method. *Phys. Rev. B* **50**, 17953–17979 (1994).
37. Perdew, J. P., Ernzerhof, M. & Burke, K. Rationale for mixing exact exchange with density functional approximations. *J. Chem. Phys.* **105**, 9982–9985 (1996).
38. Wang, L., Maxisch, T. & Ceder, G. Oxidation energies of transition metal oxides within the GGA + U framework. *Phys. Rev. B* **73**, 195107 (2006).
39. Zhou, F., Marianetti, C. A., Cococcioni, M., Morgan, D. & Ceder, G. Phase separation in  $\text{Li}_x\text{FePO}_4$  induced by correlation effects. *Phys. Rev. B* **69**, 201101 (2004).
40. Kirklin, S. et al. The Open Quantum Materials Database (OQMD): assessing the accuracy of DFT formation energies. *npj Comput. Mater* **1**, 15010–15024 (2015).
41. Saal, J. E., Kirklin, S., Aykol, M., Meredig, B. & Wolverton, C. Materials design and discovery with high-throughput density functional theory: The Open Quantum Materials Database (OQMD). *JOM* **65**, 1501–1509 (2013).

## Acknowledgements

This work was supported by the Centre for Electrochemical Energy Science, an Energy Frontier Research Centre funded by the US Department of Energy, Office of Science, Office of Basic Energy Sciences under award number DE-AC02-06CH11. Use of the Advanced Photon Source and the Centre for Nanoscale Materials, both Office of Science user facilities operated for DOE, Office of Science by Argonne National Laboratory, was supported by the US DOE under Contract No. DE-AC02-06CH11357. The authors acknowledge C.-K. Lin and X. Wang for preparing the  $\text{Li}_3\text{FeO}_4$  powders and electrodes. L.L. and M.K.Y.C. thank E. Shirley and J. Vinson for the use of and guidance with the OCEAN code. The computing resources are supported by the National Energy Research Scientific Computing Center, a DOE Office of Science User Facility supported by the Office of Science of the US Department of Energy under Contract DE-AC02-05CH11231, and Blues, a high-performance computing cluster operated by the Laboratory Computing Resource Center at Argonne National Laboratory.

## Author contributions

C.Z. and J.L. conceived the idea and design of the experiments. Z.Y. and C.W. performed the DFT simulations. L.M. and T.W. carried out the measurements and analysis of XAS. V.A.M. performed the fitting of Raman spectra. J.W. performed the TEM imaging. L.L. and M.K.Y.C. performed the oxygen core-level spectrum simulations. E.L. and E.E.A. performed the measurements and analysis of ex situ Mössbauer spectroscopy. Y.R. contributed to measurements of in situ and ex situ XRD. C.J. and M.M.T. contributed to discussions and interpretation of the data. The project was supervised by J.L. and K.A.

## Competing interests

The authors declare no competing financial interests.

## Additional information

**Supplementary information** is available for this paper at <https://doi.org/10.1038/s41560-017-0043-6>.

**Reprints and permissions information** is available at [www.nature.com/reprints](http://www.nature.com/reprints).

**Correspondence and requests for materials** should be addressed to J.L. or C.W. or K.A.

**Publisher's note:** Springer Nature remains neutral with regard to jurisdictional claims in published maps and institutional affiliations.